



# Light-induced current mapping in oxide based solar cells with nanoscale resolution

Shrabani Panigrahi\*, Tomás Calmeiro, Rodrigo Martins, Elvira Fortunato\*

Departamento de Ciência dos Materiais, CENIMAT/i3N, Faculdade de Ciências e Tecnologia–Universidade Nova de Lisboa and CEMOP/Uninova, 2829-516 Caparica, Portugal

## ARTICLE INFO

### Keywords:

ZnO nanorods/Cu<sub>2</sub>O  
Seed layer  
Photoconductive AFM  
Photoresponse  
Nanoscale resolution

## ABSTRACT

Transport properties of photo-induced charge carriers through different grains in the polycrystalline photovoltaic devices strongly depend on the microstructural pattern of the active layers. Therefore, photocurrent mapping with nanoscale resolution is important to know about the electrical responses of the different grains in the polycrystalline photovoltaic devices. Here, we have used photoconductive atomic force microscopy for mapping the photocurrent with nanoscale resolution of two types of ZnO nanorods/Cu<sub>2</sub>O based solar cells. The morphology and current have been measured simultaneously with nanoscale resolution from the top surfaces of the devices at different applied voltages. It is demonstrated that the nanostructure of the active layers is one of the most important variables determining device performances. Different local photovoltaic performances have been observed from these two devices due to various microstructural and electrical phenomena of their seed layers. On the other hand, significant variations in short-circuit current have been observed from different grains of the devices which appeared more alike in the micrograph owing to various transport properties of photo-carriers. It is observed that the grain boundaries are more preferable for charge collection over the grain interiors. It shows a higher short circuit current close to the boundary than the grain inside. This study illustrates an important area for future fundamental research to enhance the performances of the polycrystalline photovoltaic devices through better control of morphology and improving the inherent properties of the active layers.

## 1. Introduction

Utilizing solar power through converting electrical energy by a solar cell or photovoltaic cell is a suitable way to provide the world's consistently growing energy needs [1–4]. The improvement in solar cell technology from silicon based solar cells to further developments in thin films solar cells, dye sensitized solar cells, organic solar cells and perovskite solar cells show an enhancement in cell efficiency day by day [5–9]. The conversion efficiency of a solar cell depends on the spectrum and intensity of the incident light as well as the microstructure and inherent properties of the active layers [10–12]. The research to optimize the manufacturing process to improve the microstructural and intrinsic properties of the active layers has a vital significance in the performance of a solar cell. In case of thin film solar cells, active layers are composed of nano-sized crystalline grains and their interfaces, *i.e.* boundaries which induce microscopic dislocations, vacancies, and indistinct bonds [13]. Therefore, the properties in the nanoscale range are different for different grain interiors (GI) and grain boundaries (GB). According to these points, the local photovoltaic performances would

be different from one grain to another. In a macroscopic scale, the obtained efficiency of the bulk heterojunction solar cell is the whole combination of the local photovoltaic performances of the different grains. Hence, to improve the performances of the bulk heterojunction solar cells, it is important to know the local photovoltaic performances of the different grains. There are some reports on the large scale imaging techniques like laser beam induced current (LBIC) mapping, light beam induced current (LBIC) mapping used to characterize the photovoltaic performances of the different cells [14–16]. Alternatively, different microscopic techniques such as transmission electron microscopy (TEM), atomic force microscopy (AFM), and scanning transmission X-ray microscopy (STXM) have been used to study the morphology of the nanostructured materials [17–19]. However, these systems can only provide the information about the microstructure of the film not about the photovoltaic performances of the individual grain in the micrographs. In this context, photoconductive atomic force microscopy (pc-AFM), a nanoscale imaging method, allows to establish the direct correlations between the morphology and the electrical responses of the different grains. It is used to map the local photocurrent and the

\* Corresponding authors.

E-mail addresses: [spqdot@gmail.com](mailto:spqdot@gmail.com) (S. Panigrahi), [emf@fct.unl.pt](mailto:emf@fct.unl.pt) (E. Fortunato).

microstructure of the film simultaneously [20–22]. Furthermore, it has been used to record the electronic information with nanoscale resolution from photovoltaic materials by applying some voltages between the conductive tip and the sample. By measuring the photocurrent as a function of applied voltages, we are able to obtain the photovoltaic parameters such as short-circuit current ( $I_{sc}$ ), open-circuit voltage ( $V_{oc}$ ) and fill factor (FF) for different grains in the nanoscale range. Recently, it has been implemented for analyzing the photovoltaic performances of different solar cells in nanoscale range [23–28]. Due to the small radius of the tip ( $\approx 25$  nm) used in the pc-AFM measurement system, photovoltaic performances can be studied with nanoscale resolution (better than 100 nm). The results are connected with the bulk device photovoltaic performances and also provide a complete picture on the charge carrier transport mechanism within different grains and boundaries in the polycrystalline photovoltaic devices.

In this report, pc-AFM has been used for mapping the local photocurrent of two oxide based solar cells with two different seed layers at various applied voltages including under short-circuit condition. By solution process technique, we have developed two different types of ZnO nanorods (NRs)/Cu<sub>2</sub>O based solar cells on un-doped ZnO and Al doped ZnO (AZO) seed layers, respectively. In oxide based solar cells, ZnO/Cu<sub>2</sub>O hetero-junction has the most constructive conduction band edge alignment for solar cell applications [29,30]. We have observed the variation in the local photovoltaic performances between two devices due to different microstructural and electrical properties of their seed layers. On the other hand, a surprising range of photocurrents has been detected from different grains of the devices, which are appearing more similar in the topography image. In macroscopic scale, we have always studied the photovoltaic performances for bulk heterojunction solar cells having different seed layers. Here, the observation of local photoresponses in solar cells is significant to know the basic photovoltaic mechanism inside the cells depending on the microstructure and other features of the active layers.

## 2. Experimental details

### 2.1. Materials

ITO coated glass substrate, zinc acetate di-hydrate [Zn(CH<sub>3</sub>COO)<sub>2</sub>·2H<sub>2</sub>O], Aluminium chloride (AlCl<sub>3</sub>·6H<sub>2</sub>O), methanol (solvent), acetic acid (catalyst), hexamethylenetetramine [(CH<sub>2</sub>)<sub>6</sub>N<sub>4</sub>], copper(II) acetate monohydrate (Cu(CH<sub>3</sub>COO)<sub>2</sub>·H<sub>2</sub>O), glucose (reducing agent), and isopropanol (solvent). All used chemicals (reagent grade) were purchased from Aldrich. No further purification was done; the chemicals have been used for making the cell materials. De-ionized water from Millipore equipment was used.

### 2.2. Device fabrication

ITO coated glass substrates were thoroughly washed by soap solution and then rinsed by de-ionized water, acetone and iso-propanol, respectively, and finally these were dried in a dry air stream. At first, very thin ( $\sim 40$  nm) seed layer was deposited on the substrate by spray pyrolysis technique using a commercial spraying system (SONOTEK Exacta Coat). The substrate of ITO glass was kept at 340 °C and the precursor solution of zinc acetate di-hydrate (0.05 M) with methanol and acetic acid (mixing ratio 49:1) was sprayed on the substrate for the deposition of un-doped ZnO seed layer with a pneumatic spray nozzle (Spraying Systems Co.) at a flow rate of 1 mL/min. For Al doping, hexahydrate aluminum chloride (AlCl<sub>3</sub>·6H<sub>2</sub>O) was added in the parent solution. The Al/Zn ratio in the solution was varied from 1 at% to 4 at%. The doped seed layer (3 at%) which showed the best electrical properties was used for the next step for making the device structure.

At the next step, ZnO NRs were fabricated on the seed layer (un-doped and doped) assisted substrate by a chemical solution deposition process with an aqueous solution of zinc acetate di-hydrate and

hexamethylenetetramine. The seed layer assisted substrates were immersed in that solution for 3 h at 90 °C to grow the ZnO NRs. The samples were then washed by de-ionized water and annealed under vacuum by using rapid thermal annealing (RTA) treatment at 500 °C for 1 min.

After the growth of ZnO NRs, Cu<sub>2</sub>O layer was deposited on the ZnO layer by the spray pyrolysis technique. A precursor solution of copper (II) acetate monohydrate (0.02 M) and glucose (0.03 M) dissolved in water and isopropanol (mixing ratio 4:1) was sprayed by the ultrasonic nozzle on the ZnO layer at 275 °C using a hot plate. The solution flow rate and the airflow pressure were the same at the time of seed layer deposition. Before the deposition of the contact layer, finally the heterojunction was annealed in vacuum at 500 °C for 30 s using RTA. For the bulk device measurement, Au back contacts (thickness  $\sim 150$  nm) were deposited by thermal evaporation (Vinci Technologies) technique onto the Cu<sub>2</sub>O layer using a shadow mask where each contact patch had a diameter of 1.75 mm, corresponding to an area of 0.0237 cm<sup>2</sup>.

### 2.3. Measurement details

All pc-AFM measurements were performed using an MFP-3D AFM (Asylum Research, SantaBarbara, CA) using an ORCA-2 current pre-amplifier holder operated in air. All current measurements were performed using conductive PtIr-coated silicon AFM tip (Nanoworld, CONTPT) with a resonant frequency of  $\sim 13$  kHz and force constant of  $\sim 0.2$  N m<sup>-1</sup>. The scan speed was 1 Hz and the images were acquired with a resolution of 1024  $\times$  1024 pixels. We have illuminated the device with a Fiber-Lite MI-150R light source.

To know about the surface potential, Kelvin Probe Force Microscopy (KPFM) was used with Olympus AC240TM probes (spring constant: 2 N/m, resonant frequency: 70 kHz) system in a double pass mode. We have illuminated the device by the same light source.

For electrical characterization, a digital source meter (Keithley Model 2400) was used to apply the voltages to the cell while the current was recorded. Illumination was provided through AM 1.5 illumination conditions with a Sciencetech SS1.6kW-A-2-Q system consisting of a Xe lamp with a light intensity of 100 mW cm<sup>-2</sup>. The morphological characterizations of the seed layers, ZnO NRs and ITO/ZnO/Cu<sub>2</sub>O/Au devices were performed by SEM measurements using a Carl Zeiss AURIGA Cross Beam workstation. For focused ion beam (FIB) experiments, Ga<sup>+</sup> ions were accelerated to 30 kV at 10 pA and the etching depth was kept around 1000 nm. The structural characterization of the seed layers and NRs were performed by X ray diffraction (XRD) analysis using the computer-controlled Panalytical Xpert PRO system (Cu K $\alpha$  radiation;  $\lambda = 1.5405$  Å) and X'Celerator 1D detector. The electrical properties were determined from resistivity and Hall coefficient measurement at room temperature. The electrical resistivity, carrier concentration and mobility measurement of the seed layers were done using a Hall Effect measurement system (BiO-RAD). Optical transmittance was obtained by using UV–vis–NIR spectrometer (Perkin Elmer; Lambda 950).

## 3. Results and discussion

Local photocurrent measurement was performed on the same devices which were used for bulk device photovoltaic measurement previously to correlate the performances of the devices in microscopic scale. In the beginning, current density-voltage ( $J$ - $V$ ) measurements for the bulk devices have been performed under simulated AM1.5G illumination at ambient environment using a solar simulator (Fig. S1a). The details of the photovoltaic performances for the bulk devices are in Supporting information. To know the local photocurrent responses of the solar cells, a pc-AFM measurement set-up with a sample holder and light source was used. Fig. 1 shows the schematic diagram of the planar NR based oxide solar cell mounted in a pc-AFM configuration for measuring the local photocurrent. This system is based on conductive

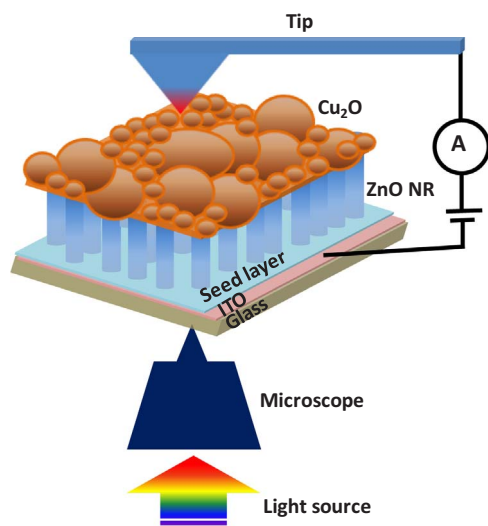


Fig. 1. Schematic diagram of the experimental set-up for pc-AFM measurement.

AFM. Voltages were applied between the ITO substrate and the conductive probe tips and the current was recorded by the AFM. The morphology and current have been measured simultaneously at different voltages at a fixed position of the sample. Fig. 2a and b show the topography and corresponding photocurrent images of the ZnO NR/Cu<sub>2</sub>O based solar cell having un-doped ZnO seed layer. Here, the small area of the device ( $2 \times 1.5 \text{ sq } \mu\text{m}$ ) is shown in these images. From the height and current images it is clear that current is higher at the GB than the GI. Fig. 2c shows a series of local current-voltage (*I*-*V*) characteristics within open circuit voltage at three different positions of the cell (shown in Fig. 2a and b) under illumination condition. Different photovoltaic performances with various  $I_{\text{SC}}$ ,  $V_{\text{OC}}$  values have been observed at three different positions of the cell. Fig. 2d represents the line profiles of the topography and photocurrent images across the selected area of the device (Fig. 2a and b). On the other hand, Fig. 2e and f show the topography and corresponding photocurrent images of another ZnO NR/Cu<sub>2</sub>O based solar cell with AZO seed layer, respectively. The same area of the device like the previous one ( $2 \times 1.5 \text{ sq } \mu\text{m}$ ) is represented in these images. Fig. 2g shows the local *I*-*V* characteristics at three different positions of the cell mentioned in the height and current images, respectively (Fig. 2e and f). The photovoltaic performances at three different positions of the cell are different due to various transport properties of the photocarriers. Fig. 2h shows the line profiles of the topography and photocurrent images across the selected area of the device (Fig. 2e and f). The line profiles for two devices also clearly represent the effective charge collection at the GB than the GI. Significantly, these images were obtained at zero applied bias representing under short-circuit condition. For un-doped seed layer based solar cells, photovoltaic parameters such as  $I_{\text{SC}}$ ,  $V_{\text{OC}}$  and FF for three different positions (Fig. 2c) are varied from 0.001 to 3.99 nA, 0.31 to 0.6 V and 0.22 to 0.38, respectively. In contrast, these photovoltaic parameters are varied from 0.001 to 10.48 nA ( $I_{\text{SC}}$ ), 0.45 to 0.51 V ( $V_{\text{OC}}$ ) and 0.22 to 0.39 (FF) for three different positions of the doped seed layer based solar cell (Fig. 2g). These results show two significant qualitative features of the devices. At first, for the doped seed layer based solar cell, photoresponses in the nanoscale range are much better than the un-doped seed layer based solar cell which is similar with the bulk device photovoltaic performances (Fig. S1a). Secondly, photoresponses are not same everywhere on the whole surface of the cells, i.e. depended on the morphology of the polycrystalline materials.

In order to explain the different features of the photovoltaic performances for two devices, we have first characterized the morphological and electrical properties of two different types of seed layers with nanoscale resolution. Fig. 3a i), ii) and iii), iv) show the 3D topography

images and photocurrent images in nanoscale range of the un-doped ZnO and AZO seed layers, respectively, collected at a fixed tip voltage. The microstructures of the two seed layers are found to be identical with dense interconnected grains. In case of the doped seed layer, the sizes of the grains become smaller than the undoped one due to the difference between the ionic radius of  $\text{Zn}^{2+}$  (74 pm) and the doping components  $\text{Al}^{3+}$  (53 pm) [31]. On the other hand, for trivalent cation doping like  $\text{Al}^{3+}$ , the concentration of the zinc interstitials are reduced for charge compensation which suppressed ZnO grain development [32]. It leads to decrease the grain size of the AZO thin films. The SEM images (Fig. S3a) clearly show the size difference of the grains between two seed layers. The photocurrent images show that the higher photocurrent is generated across the doped seed layer. The corresponding line profiles of the photocurrent (Fig. 3a (v)) across the whole area shown in the images ( $2 \times 1.5 \mu\text{m}$ ) also demonstrate the difference of the photocurrent between the doped and un-doped seed layer. The morphology, surface potential and electrical properties of the two different seed layers have been studied separately (shown in Supporting information). Al doping in ZnO matrix leads to increase the carrier concentration and decrease the resistivity. The substitution of  $\text{Zn}^{2+}$  ion with  $\text{Al}^{3+}$  produces one free electron as Al atom has one more valence electron in the outermost orbit than Zn [33]. Park et al. [34] also reported that the electrical conductivity of AZO film is higher than that of pure ZnO films due to the contribution from  $\text{Al}^{3+}$  ions instead of the  $\text{Zn}^{2+}$  ions, Al interstitial atoms, as well as from oxygen vacancies and Zn interstitial atoms. Excess electrons change the Fermi level as well as work function and surface potential of the doped seed layer (Fig. S4e). Due to the increase of free charge carriers, higher photocurrent generation has been detected in AZO seed layer than the un-doped one in nanoscale range. Additionally, the transmittance of the AZO seed layer is also better than the un-doped one in the visible region which makes easy to transmit the wide range of solar spectrum (Fig. S3b). ZnO NRs grown on these two different seed layers were also analyzed. Fig. 3b i), ii) and iii), iv) show the 3D topography images and local photocurrent images of NRs developed on un-doped ZnO and AZO seed layers, respectively, at the same tip voltage. It is clear from the topography images that the NRs on the doped seed layer are more compact and have a higher density than the un-doped one. XRD analysis (Fig. S3d) shows that the peak (002) of ZnO NRs on AZO seed layer is relatively more intense than that on the un-doped ZnO seed layer, which is a preferred c-axis orientation with a proper crystal quality. Therefore, the NRs on the un-doped ZnO seed layer have poor vertical alignment. The local photocurrent generation across the boundary of the ZnO NRs with doped seed layer (Fig. 3b iv) is much higher than that of the un-doped one (Fig. 3b iii). The corresponding line profiles of the photocurrent (Fig. 3b v) across the whole area shown in the images ( $2 \times 1.5 \mu\text{m}$ ) also confirm the same nature of the photocurrent distribution. Due to Al doping, the morphology and electrical properties of the ZnO seed layer have been improved as well as the properties of the ZnO NRs developed on this doped seed layer have also been enhanced [35–38]. So, the characteristics of the ZnO NRs are strongly dependent on the crystallinity, type, and surface properties of the seed layer. Thus, AZO seed layer modified the ZnO NRs arrays to promote the performances of the solar cells. In a hybrid solar cell, ZnO NRs play an important role to extract the charge carriers from the absorber layer and provide a fast and direct path for them. Thus, when these NRs arrays were used as a working electrode in a solar cell showed a better electron transport medium [11,39,40]. Therefore, the bulk heterojunction solar cells as well as the nanoscale devices with the doped seed layer showed enhanced photovoltaic performances.

We now turn to the discussion of the other part of our results where the variations in the local photovoltaic performances have been observed among different grains across the surfaces of the solar cell. From Fig. 2c and g, different photovoltaic performances with different  $I_{\text{SC}}$  and  $V_{\text{OC}}$  values have been observed at three various positions for both devices. There are several explanations of the observed inconsistency in

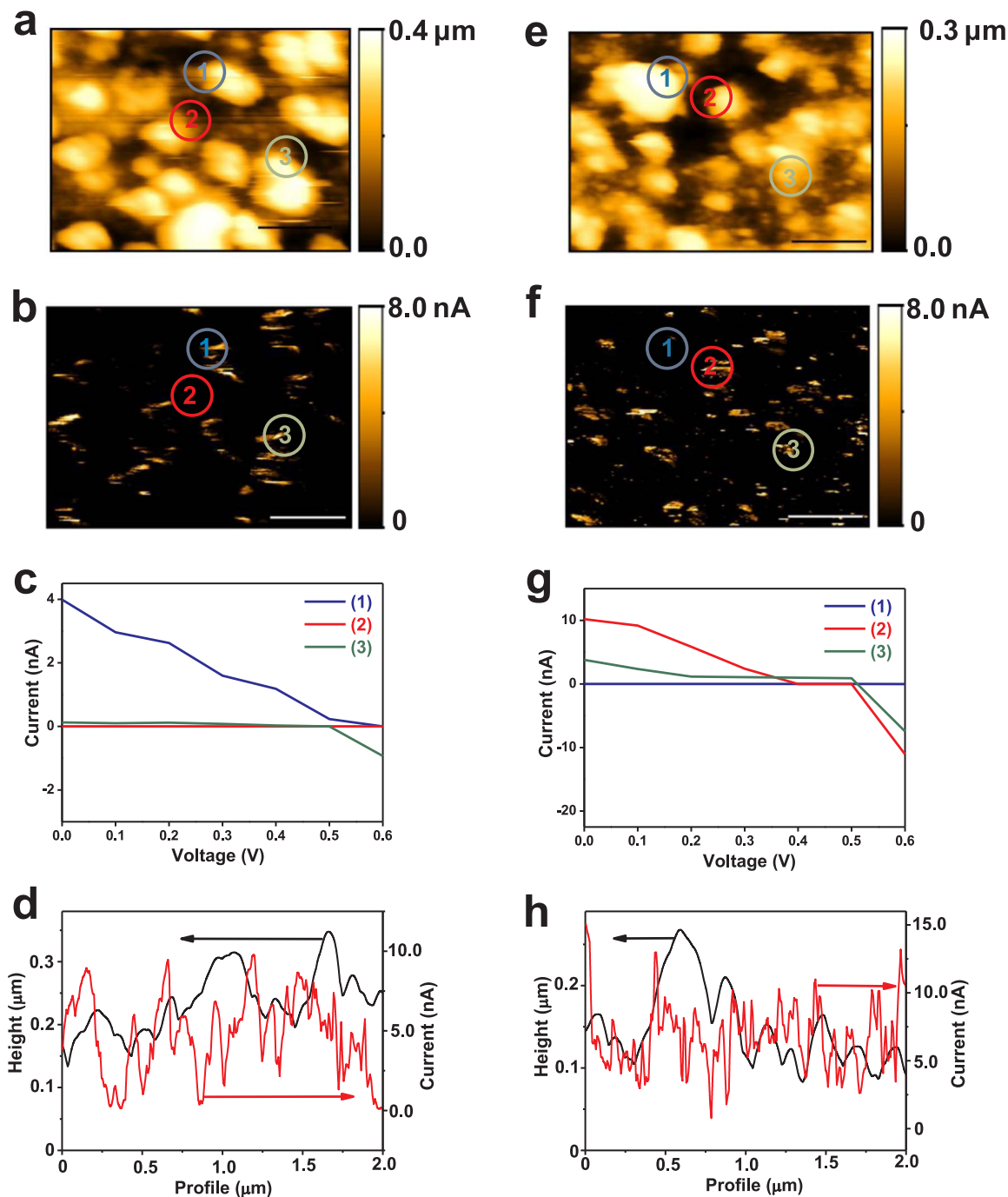


**Fig. 2.** a) and b) AFM height image and photocurrent map measured at zero external bias from the top surface of the un-doped seed layer based ZnO NRs/Cu<sub>2</sub>O solar cell (scale bar = 500 nm). c) Local current-voltage (*I*-*V*) data acquired at three locations indicated in a and b. d) Line profiles along the topography and corresponding photocurrent map images (across the whole area shown in the images) as indicated by black and red lines in the graph for un-doped seed layer based cell. e) and f) AFM height image and photocurrent map measured from the top surface of the doped seed layer based ZnO NRs/Cu<sub>2</sub>O solar cell at zero external bias (scale bar = 500 nm). g) Local current-voltage (*I*-*V*) data acquired at three locations indicated in e and f. h) Line profiles along the topography and corresponding photocurrent map images (across the whole area shown in the images) as indicated by black and red lines in the graph for doped seed layer based cell. (For interpretation of the references to color in this figure legend, the reader is referred to the web version of this article.)

the local photovoltaic performances across the different grains of the polycrystalline devices [13,24]. Polycrystalline materials are composed of many grains with distinct crystallographic orientations [23], different absorption and transport properties which may influence the photocurrent responses of the grains. We already mentioned that the grain boundaries induce microscopic dislocations, vacancies, and distorted bonds. So, the extra electronic states have an effect on the recombination and transport properties of majority and minority charge carriers, and consequently on the overall performances of the polycrystalline devices [41–44]. On the other hand, the presence of surface

contaminants may also affect the photocurrent signal. Fig. 2d and h show the variations of the photocurrent between the GB and GI of the materials due to inhomogeneities inside them [25]. These profiles show that charge collected more efficiently at the GB than the GI because GB are local collectors of the minority carriers [25]. These are related to the difference of the work function between the GB and the GI. Fig. 4a and b represent the topography and corresponding contact potential difference (CPD) images of the Cu<sub>2</sub>O surface. On this basis, surface potential image obtained by KPFM shows a lower CPD at the GI than the GB (indicated by the circle 1 and 2 in Fig. 4b) related to a



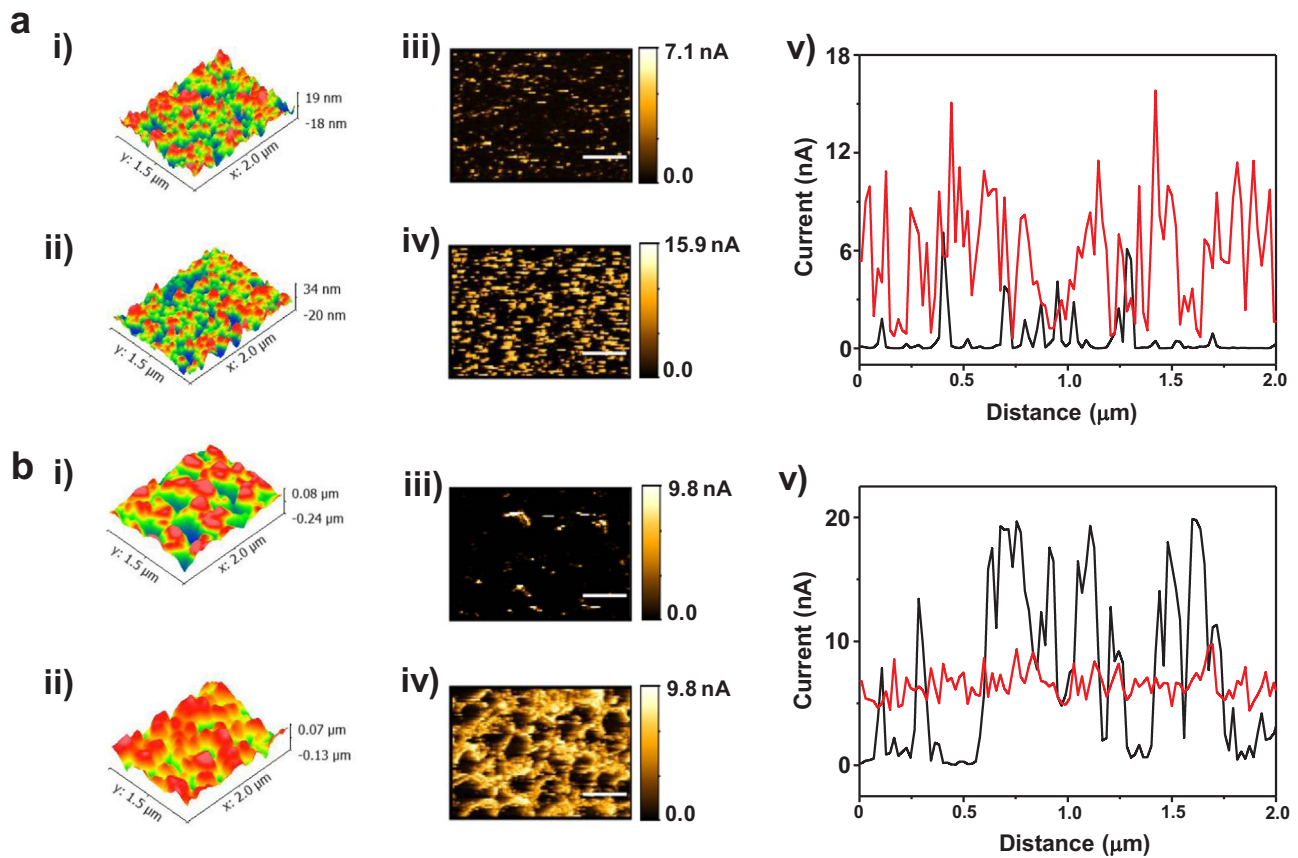


**Fig. 3.** a i) and ii) 3D topography images of ZnO and AZO seed layers, respectively. iii) and iv) Corresponding photocurrent map of ZnO and AZO seed layers, respectively (scale bar = 500 nm). v) Line profiles of the photocurrent of ZnO (black line) and AZO (red line) seed layers (across the whole area shown in the images). b i) and ii) 3D Topography images of ZnO NRs grown on un-doped ZnO and AZO seed layers, respectively. iii) and iv) Corresponding photocurrent map of ZnO NRs on un-doped ZnO and AZO seed layers, respectively (scale bar = 500 nm). v) Line profiles of the photocurrent of ZnO NRs grown on un-doped ZnO (black line) and AZO seed layers (red line), respectively (across the whole area shown in the images). (For interpretation of the references to color in this figure legend, the reader is referred to the web version of this article.)

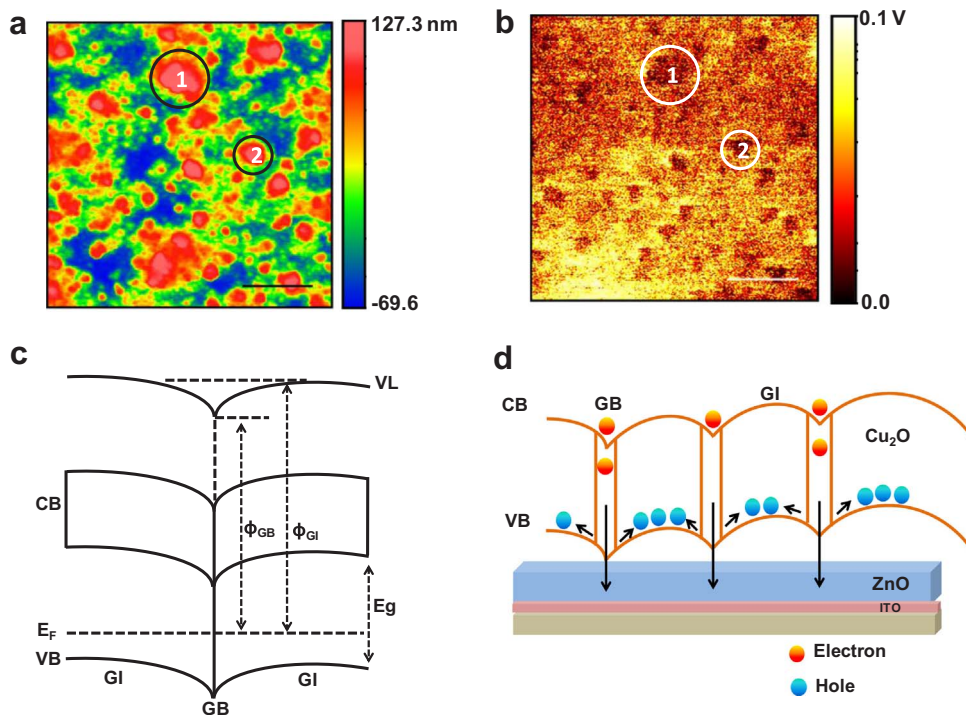


**Fig. 4.** a) and b) Topography and corresponding CPD images of Cu<sub>2</sub>O layer (scale bar 500 nm). c) The schematics of band diagram around GB in Cu<sub>2</sub>O thin film. d) The schematic diagram showing the electron and hole flow direction in the ZnO NRs/Cu<sub>2</sub>O based device structure.

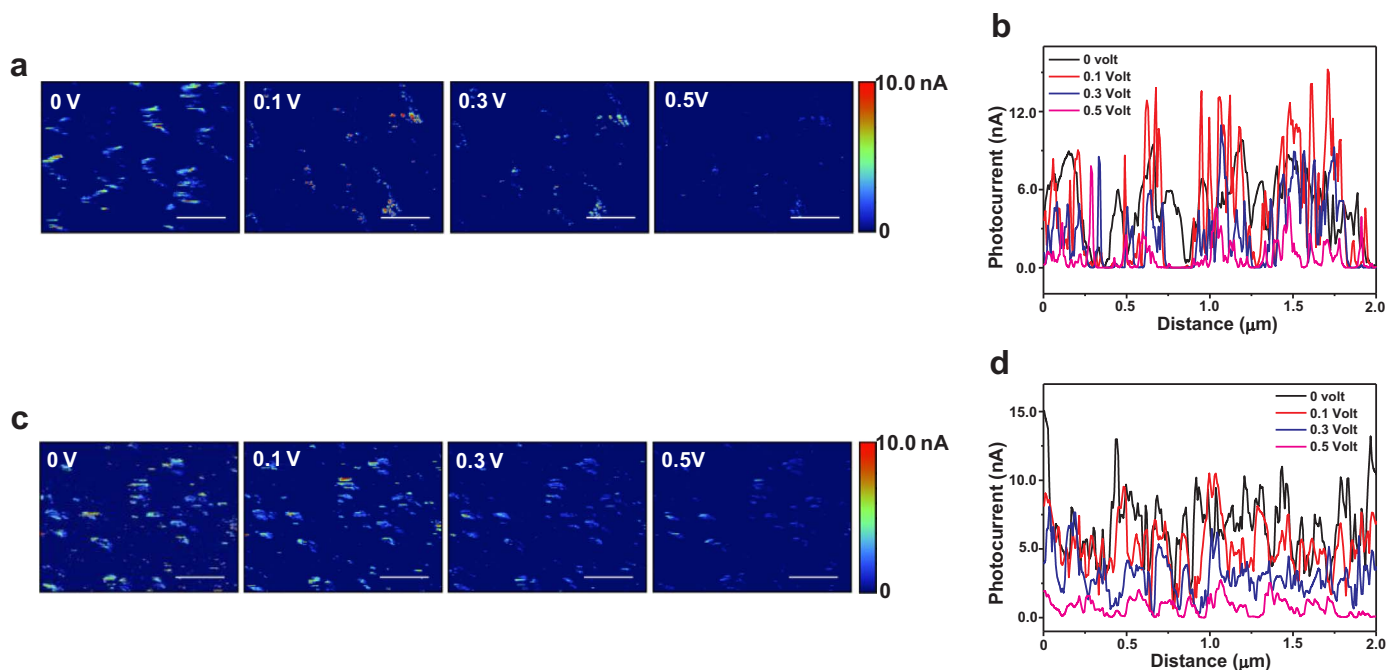


Fig. 5. a) Photocurrent images taken from un-doped ZnO seed layer based ZnO NRs/Cu<sub>2</sub>O solar cell and b) line profiles of the photocurrent at different voltages. c) Photocurrent images taken from AZO seed layer based ZnO NRs/Cu<sub>2</sub>O solar cell and d) line profiles of the photocurrent at different voltages.

downward band-bending of the energy band diagram at the GB (Fig. 4c). This directs minority carriers, *i.e.* electrons in the p-type absorber material (Cu<sub>2</sub>O) attracted into the GB, and majority carriers, holes repelled away from the GB (Fig. 4d) which suppress the recombination rate of the carriers. Therefore, holes come together in the GI and it works as the best channel for the transport of majority carriers into the back electrode. The variations in the local charge transport across different grains have a significant effect on the bulk device photovoltaic performances.

Further than acquiring the photocurrent images at zero bias condition, local photovoltaic performances of the devices can be methodically studied within short-circuit and open circuit conditions at the same position of the devices. Fig. 5 represents the local photocurrent images and the corresponding line profiles for un-doped and doped ZnO seed layer based devices at some specific voltages. Fig. 5a shows the photocurrent images of the un-doped ZnO seed layer based solar cell at some positive voltages between 0 to 0.5 V (near the open-circuit voltage). The current values across the domain of the cell are slowly decreased by increasing the forward bias within open circuit voltage. The average current across the small area of the device ( $2 \times 1.5 \mu\text{m}$ ) are given by  $(4.754 \pm 2.454) \text{ nA}$ ,  $(4.282 \pm 4.092) \text{ nA}$ ,  $(2.472 \pm 2.601) \text{ nA}$  and  $(0.8382 \pm 1.125) \text{ nA}$  at 0 V, 0.1 V, 0.3 V and 0.5 V, respectively. Fig. 5b shows the corresponding line profiles of the local photocurrent images. Similarly, for AZO seed layer based solar cell, the local photocurrent images are shown in Fig. 5c at different voltages. The average current over the area shown in these images ( $2 \times 1.5 \mu\text{m}$ ) are given by  $(6.731 \pm 2.309) \text{ nA}$ ,  $(5.196 \pm 1.907) \text{ nA}$ ,  $(3.035 \pm 1.419) \text{ nA}$  and  $(0.7814 \pm 0.5951) \text{ nA}$  at 0 V, 0.1 V, 0.3 V and 0.5 V, respectively. Fig. 5d shows the corresponding line profiles of the local photocurrent images. At zero applied bias, under illumination, photons were absorbed and disassociated at the interface of the active layers. Due to the built in potential, electrons and holes flow to the cathode and anode, respectively, and thus produce photocurrent. After that when a forward bias was applied which generated a current in the opposite direction of the photocarriers generated current and compensated it. Thus, at a certain voltage, it shows the zero current indicating  $V_{OC}$ . During photocurrent mapping under different voltages, the device position was fixed in order to show the change in the local photoresponses across the

different grains with respect to applied voltages. At the imaging time, the measured photocurrent may be reduced due to damage at the local position being probed. So, to deal with this concern, the AFM height images of the top surfaces of the devices at different applied voltages throughout the photocurrent measurement are shown in Supporting information (Fig. S5). These images show that there is no damage created throughout the film due to probing. Therefore, significant variations in the local photovoltaic performances have been observed between two devices. Due to doping, the electron density and the conductivity of AZO seed layer become more improved and the NRs developed on this doped seed layer also showed the higher current than the un-doped one at the same voltage. All the layers in the doped seed layer based devices showed pronounced photoresponse under illumination, so the doped seed layer can be qualified as an improved visible light absorption and efficient interfacial charge transport medium. Nayeri et al. also observed the enhanced property of ZnO NWs grown on AZO seed layer than that on ZnO seed layer in macroscopic scale [45]. The new insight added from this research work that we can develop highly efficient oxide based solar cells in future by doing nanostructuring effects in the active layers, such as making 3D nanostructures for better carrier transport or improving the inherent properties of the materials by doping.

#### 4. Conclusions

In conclusion, pc-AFM has been used here for mapping the local photoresponses of two different types of oxide based solar cells developed on un-doped and doped seed layers, respectively. The local photovoltaic performances in terms of traditional photovoltaic parameters such as  $I_{SC}$ ,  $V_{OC}$  and FF are correlated with the bulk device photovoltaic performances. Obviously, these data are not directly equal with the bulk device photovoltaic parameters because those devices have a large contact area. The photocurrent variations in nanoscale range have been observed in two ways. At first, significant variations in the local photovoltaic performances have been observed between two devices due to their different seed layers. Secondly, there are large variations in the photocurrent within different grains which are identical in the topography image. The immediate change in the photocurrent from one

grain to another is due to different transport mechanism of the photo-carriers through the GI and the GB. In order to find out the origin of the nanoscale variations of photovoltaic performances, the microstructure and local photoresponses for all layers of the devices have been studied sequentially. The topography and local photocurrent images of the layers helped us a lot to explain the cause of the enhanced photovoltaic performances of the doped seed layer based solar cell than the undoped one. From this study, the importance of the nanoscale observation of the photovoltaic performances for oxide based solar cells is highlighted. The results reveal that bulk device performances can be enhanced through better control of morphology and improving the inherent properties of the active layers.

## Acknowledgements

This study was funded by the European Commission under the FP7 All Oxide PV project “Novel Composite Oxides by Combinatorial Material Synthesis for Next Generation All-Oxide-Photovoltaics” number 309018 and the FP7 ERC AdG project “Transparent Electronics” number 228144. This work was partially supported by FEDER funds through the COMPETE 2020 Programme and National Funds through FCT – Portuguese Foundation for Science and Technology under the project UID/CTM/50025/2013.

## Appendix A. Supporting information

Supplementary data associated with this article can be found in the online version at <http://dx.doi.org/10.1016/j.solmat.2017.10.012>.

## References

- [1] H. Tsai, W. Nie, J.-C. Blancon, C.C. Stoumpos, R. Asadpour, B. Harutyunyan, A.J. Neukirch, R. Verduzco, J.J. Crochet, S. Tretiak, L. Pedesseau, J. Even, M.A. Alam, G. Gupta, J. Lou, P.M. Ajayan, M.J. Bedzyk, M.G. Kanatzidis, A.D. Mohite, High-efficiency two-dimensional Ruddlesden–Popper perovskite solar cells, *Nature* 536 (2016) 312–316.
- [2] M. Kaltenbrunner, G. Adam, E.D. Glowacki, M. Drack, R. Schwoedlauer, L. Leonat, D.H. Apaydin, H. Groiss, M.C. Scharber, M.S. White, N.S. Sariciftci, S. Bauer, Flexible high power-per-weight perovskite solar cells with chromium oxide-metal contacts for improved stability in air, *Nat. Mater.* 14 (2015) 1032–1039.
- [3] X. Miao, S. Tongay, M.K. Petterson, K. Berke, A.G. Rinzier, B.R. Appleton, A.F. Hebard, High efficiency graphene solar cells by chemical doping, *Nano Lett.* 12 (2012) 2745–2750.
- [4] A. Guerrero, J. You, C. Aranda, Y.S. Kang, G. Garcia-Belmonte, H. Zhou, J. Bisquert, Y. Yang, Interfacial degradation of planar lead halide perovskite solar cells, *ACS Nano* 10 (2016) 218–224.
- [5] F. Bella, S. Galliano, M. Falco, G. Viscardi, C. Barolo, M. Gratzel, C. Gerbaldi, Approaching truly sustainable solar cells by the use of water and cellulose derivatives, *Green Chem.* 19 (2017) 1043–1051.
- [6] M. Gerosa, A. Sacco, A. Scalia, F. Bella, A. Chiodoni, M. Quaglio, E. Tresso, S. Bianco, Toward totally flexible dye-sensitized solar cells based on titanium grids and polymeric electrolyte, *IEEE J. Photovolt.* 6 (2016) 498–505.
- [7] S. Wang, S. Yan, M. Wang, L. Chang, J. Wang, Z. Wang, Construction of nanowire  $\text{CH}_3\text{NH}_3\text{PbI}_3$ -based solar cells with 17.62% efficiency by solvent etching technique, *Sol. Energy Mater. Sol. Cells* 167 (2017) 173–177.
- [8] J.D. Major, L.J. Phillips, M. Al Turkestani, L. Bowen, T.J. Whittles, V.R. Dhanak, K. Durose, P3HT as a pinhole blocking back contact for CdTe thin film solar cells, *Sol. Energy Mater. Sol. Cells* 172 (2017) 1–10.
- [9] D. Pintossi, G. Iannaccone, A. Colombo, F. Bella, M. Välimäki, K.-L. Väisänen, J. Hast, M. Levi, C. Gerbaldi, C. Dragonetti, S. Turri, G. Griffini, Luminescent downshifting by photo-induced sol-gel hybrid coatings: accessing multifunctionality on flexible organic photovoltaics via ambient temperature material processing, *Adv. Electron. Mater.* 2 (2016) 1–11 1600288.
- [10] K.H. Kim, M.S. Kim, B.T. Ahn, J.H. Yun, K. HoonYoon, in: *Proceedings of the IEEE Photovoltaic Energy Conversion*, 2006, pp. 575–578.
- [11] F.D. Nayeri, E.A. Soleimani, F. Salehi, Synthesis and characterization of ZnO nanowires grown on different seed layers: the application for dye-sensitized solar cells, *Renew. Energy* 60 (2013) 246–255.
- [12] M.-S. Su, C.-Y. Kuo, M.-C. Yuan, U.S. Jeng, C.-J. Su, K.-H. Wei, Improving device efficiency of polymer/fullerene bulk heterojunction solar cells through enhanced crystallinity and reduced grain boundaries induced by solvent additives, *Adv. Mater.* 23 (2011) 3315–3319.
- [13] J.-J. Li, J.-Y. Ma, Q.-Q. Ge, J.-S. Hu, D. Wang, L.-J. Wan, Microscopic investigation of grain boundaries in organolead halide perovskite solar cells, *ACS Appl. Mater. Interfaces* 7 (2015) 28518–28523.
- [14] Y. Galagan, B. Zimmermann, E.W.C. Coenen, M. Jørgensen, D.M. Tanenbaum, F.C. Krebs, H. Gortler, S. Sabik, L.H. Slooff, S.C. Veenstra, J.M. Kroon, R. Andriessen, Current collecting grids for ITO-free solar cells, *Adv. Energy Mater.* 2 (2012) 103–110.
- [15] T.W. Jones, K. Feron, K.F. Anderson, B.C. Duck, G.J. Wilson, An applied light-beam induced current study of dye-sensitized solar cells: photocurrent uniformity mapping and true photoactive area evaluation, *J. Appl. Phys.* 116 (2014) 1–9 043104.
- [16] Z. Song, A. Abate, S.C. Watthage, G.K. Liyanage, A.B. Phillips, U. Steiner, M. Graetzel, M.J. Heben, Perovskite solar cell stability in humid air: partially reversible phase transitions in the  $\text{PbI}_2\text{-CH}_3\text{NH}_3\text{I-H}_2\text{O}$  system, *Adv. Energy Mater.* 6 (2016) 1–7 1600846.
- [17] H. Hoppe, N.S. Sariciftci, Morphology of polymer/fullerene bulk heterojunction solar cells, *J. Mater. Chem.* 16 (2006) 45–61.
- [18] Y. Leprince-Wang, K. Yu-Zhang, Study of the growth morphology of TiO<sub>2</sub> thin films by AFM and TEM, *Surf. Coat. Technol.* 140 (2001) 155–160.
- [19] K.B. Burke, A.J. Stapleton, B. Vaughan, X. Zhou, A.L.D. Kilcoyne, W.J. Belcher, P.C. Dastoor, Scanning transmission X-ray microscopy of polymer nanoparticles: probing morphology on sub-10 nm length scales, *Nanotechnology* 22 (2011) 1–6 265710.
- [20] D. Wood, I. Hancox, T.S. Jones, N.R. Wilson, Quantitative nanoscale mapping with temperature dependence of the mechanical and electrical properties of poly(3-hexylthiophene) by conductive atomic force microscopy, *J. Phys. Chem. C* 119 (2015) 11459–11467.
- [21] Y. Son, Q.H. Wang, J.A. Paulson, C.J. Shih, A.G. Rajan, K. Tvrđy, S. Kim, B. Alfeeli, R.D. Braatz, M.S. Strano, Layer number dependence of MoS<sub>2</sub> photoconductivity using photocurrent spectral atomic force microscopic imaging, *ACS Nano* 9 (2015) 2843–2855.
- [22] M. Madl, W. Brezna, B. Basnar, M. Yarema, W. Heiss, J. Smoliner, Variable wavelength photocurrent mapping on PbS quantum dot: fullerene thin films by conductive atomic force microscopy, *Semicond. Sci. Technol.* 26 (2011) 1–6 095002.
- [23] Y. Kutes, Y. Zhou, J.L. Bosse, J. Steffes, N.P. Padture, B.D. Huey, Mapping the photoresponse of  $\text{CH}_3\text{NH}_3\text{PbI}_3$  hybrid perovskite thin films at the nanoscale, *Nano Lett.* 16 (2016) 3434–3441.
- [24] D.C. Coffey, O.G. Reid, D.B. Rodovsky, G.P. Bartholomew, D.S. Ginger, Mapping local photocurrents in polymer/fullerene solar cells with photoconductive atomic force microscopy, *Nano Lett.* 7 (2007) 738–744.
- [25] M.S. Leite, M. Abashin, H.J. Lezec, A. Gianfrancesco, A.A. Talin, N.B. Zhitenev, Nanoscale imaging of photo current and efficiency in CdTe solar cells, *ACS Nano* 8 (2014) 11883–11890.
- [26] B.J. Leever, M.F. Durstock, M.D. Irwin, A.W. Hains, T.J. Marks, L.S.C. Pingree, M.C. Hersam, Spatially resolved photocurrent mapping of operating organic photovoltaic devices using atomic force photovoltaic microscopy, *Appl. Phys. Lett.* 92 (2008) 013302-013302-3.
- [27] B.H. Hamadani, S. Jung, P.M. Haney, L.J. Richter, N.B. Zhitenev, Origin of nanoscale variations in photoresponse of an organic solar cell, *Nano Lett.* 10 (2010) 1611–1617.
- [28] Z.X. Zhao, X.Y. Chen, H.Q. Wu, X.M. Wu, G.Z. Cao, Probing the photovoltage and photocurrent in perovskite solar cells with nanoscale resolution, *Adv. Funct. Mater.* 26 (2016) 3048–3058.
- [29] M. Tadatsugu, N. Yuki, M. Toshihiro, N. Jun-ichi, High-efficiency oxide solar cells with ZnO/Cu<sub>2</sub>O heterojunction fabricated on thermally oxidized Cu<sub>2</sub>O sheets, *Appl. Phys. Exp.* 4 (2011) 062301.
- [30] S. Panigrahi, D. Nunes, T. Calmeiro, K. Kardarian, R. Martins, E. Fortunato, Oxide-based solar cell: impact of layer thicknesses on the device performance, *ACS Comb. Sci.* 19 (2017) 113–120.
- [31] P. Nunes, E. Fortunato, P. Tonello, F. Braz Fernandes, P. Vilarinho, R. Martins, Effect of different dopant elements on the properties of ZnO thin films, *Vacuum* 64 (2002) 281–285.
- [32] S. Fujihara, A. Suzuki, T. Kimura, Ga-doping effects on electrical and luminescent properties of ZnO:(La,Eu)OF red phosphor thin films, *J. Appl. Phys.* 94 (2003) 2411–2416.
- [33] S.P. Shrestha, R. Ghimire, J.J. Nakarmi, Y.-S. Kim, S. Shrestha, C.-Y. Park, J.-H. Boo, Properties of ZnO:Al films prepared by spin coating of aged precursor solution, *Bull. Korean Chem. Soc.* 31 (2010) 112–115.
- [34] K.C. Park, D.Y. Ma, K.H. Kim, The physical properties of Al-doped zinc oxide films prepared by RF magnetron sputtering, *Thin Solid Films* 305 (1997) 201–209.
- [35] H.K. Lee, M.S. Kim, J.S. Yu, Effect of AZO seed layer on electrochemical growth and optical properties of ZnO nanorod arrays on ITO glass, *Nanotechnology* 22 (2011) 1–8 445602.
- [36] A. Peic, T. Dimopoulos, R. Resel, S. Abermann, M. Postl, E.J.W. List, H. Brueckl, Effect of AZO substrates on self-seeded electrochemical growth of vertically aligned ZnO nanorod arrays and their optical properties, *J. Nanomater.* 2012 (2012) 1–14.
- [37] S. Lin, H. Hu, W. Zheng, Y. Qu, F. Lai, Growth and optical properties of ZnO nanorod arrays on Al-doped ZnO transparent conductive film, *Nanoscale Res. Lett.* 8 (2013) 1–6 158.
- [38] A.-I. Danciu, V. Musat, T. Busani, J.V. Pinto, R. Barros, A.M. Rego, A.M. Ferrara, P.A. Carvalho, R. Martins, E. Fortunato, Uniform arrays of ZnO 1D nanostructures grown on Al: ZnO seeds layers by hydrothermal method, *J. Nanosci. Nanotechnol.* 13 (2013) 6701–6710.
- [39] K.H. Kim, K. Utiashiro, Y. Abe, M. Kawamura, Structural properties of zinc oxide nanorods grown on Al-doped zinc oxide seed layer and their applications in dye-sensitized solar cells, *Materials* 7 (2014) 2522–2533.
- [40] S.-H. Lee, S.-H. Han, H.S. Jung, H. Shin, J. Lee, J.-H. Noh, S. Lee, I.-S. Cho, J.-K. Lee, J. Kim, H. Shin, Al-doped ZnO thin film: a new transparent conducting layer for ZnO nanowire-based dye-sensitized solar cells, *J. Phys. Chem. C* 114 (2010) 7185–7189.
- [41] J.B. Li, V. Chawla, B.M. Clemens, Investigating the role of grain boundaries in CZTS and CZTSSe thin film solar cells with scanning probe microscopy, *Adv. Mater.* 24

- (2012) 720–723.
- [42] J.S. Yun, A. Ho-Baillie, S. Huang, S.H. Woo, Y. Heo, J. Seidel, F. Huang, Y.-B. Cheng, M.A. Green, Benefit of grain boundaries in organic–inorganic halide planar perovskite solar cells, *J. Phys. Chem. Lett.* 6 (2015) 875–880.
- [43] W.K. Metzger, M. Gloeckler, The impact of charged grain boundaries on thin-film solar cells and characterization, *J. Appl. Phys.* 98 (2005) 063701-063701-10.
- [44] H. Li, X.X. Liu, Y.S. Lin, B. Yang, Z.M. Du, Enhanced electrical properties at boundaries including twin boundaries of polycrystalline CdTe thin-film solar cells, *Phys. Chem. Chem. Phys.* 17 (2015) 11150–11155.
- [45] F. Dehghan Nayeri, E. Asl Soleimani, Influence of seed layers on the vertical growth of ZnO nanowires by low-temperature wet chemical bath deposition on ITO-coated glass substrate, *Exp. Tech.* 38 (2014) 13–20.